water

MDPI

Article

Water Quality Trends and Remote Sensing Model Development in Portuguese Reservoirs Using Sentinel-2 Imagery

Geissielen A. Lauriuchi [1,2], Catarina Guimarães [2], Giorgio Pace [3,4], Gabriel R. Caballero [5], Xavier Sòria-Perpinyà [5], Marcelo Pompêo [6], Jesús Delegido [5] and Sara C. Antunes [2,7,*]

1 Institute of Science and Technology, São Paulo State University "Júlio de Mesquita Filho" (UNESP), Sorocaba 18087-180, Brazil; geissialauriuchi@gmail.com
2 Department of Biology, Faculty of Sciences, University of Porto, Rua do Campo Alegre S/N, 4169-007 Porto, Portugal; catarina.guimaraes@fc.up.pt
3 Associate Laboratory Aquatic Research Network (ARNET), Centre of Molecular and Environmental Biology (CBMA), Department of Biology, University of Minho, 4710-057 Braga, Portugal; giorgio.pace@bio.uminho.pt
4 Institute of Science and Innovation for Bio-Sustainability (IB-S), University of Minho, Rua da Universidade, 4710-057 Braga, Portugal
5 Image Processing Laboratory, Universitat de València, C/Catedrático José Beltrán Martínez, 2, 46980 València, Spain; gabriel.caballero@uv.es (G.R.C.); javier.soria-perpina@uv.es (X.S.-P.); jesus.delegido@uv.es (J.D.)
6 Limnology Laboratory, Department of Ecology, Institute of Biosciences (IB), São Paulo University (USP), São Paulo 05508-090, Brazil; mpompeo@ib.usp.br
7 CIIMAR/CIMAR LA, Interdisciplinary Centre of Marine and Environmental Research, University of Porto, Terminal de Cruzeiros do Porto de Leixões, 4450-208 Matosinhos, Portugal
* Correspondence: scantunes@fc.up.pt

Abstract

Iberian reservoirs are highly vulnerable to droughts, warming temperatures, and agricultural runoff, which accelerate eutrophication. Monitoring these dynamics is crucial for sustainable management. This study investigated long-term trends in chlorophyll-a (Chl-a) and water transparency Secchi depth and developed empirical models for the Alto Rabagão (Rb) and Aguieira (Ag) reservoirs in Portugal. We used Sentinel-2 Level-2A reflectance data coupled with 153 in situ observations (2014–2024) for model calibration (n = 95) and validation (n = 58). Temporal trends were assessed using linear regression and Mann–Kendall analyses. Empirical models based on spectral indices (TBDO1, TBDO, MCI, NDWI) were evaluated using walk-forward time-series cross-validation. Results revealed a significant Chl-a increase (0.38 µg L^{-1} $year^{-1}$; p = 0.016) and a simultaneous decline in transparency ($p < 0.001$) in Rb, indicating progressive eutrophication. In contrast, no significant trends were detected in Ag. Reservoir-specific models achieved moderate-to-high predictive performance, particularly for Chl-a (R^2 up to 0.75; cross-validated R^2 = 0.67–0.68, RMSE = 1.1 µg L^{-1}, MAE = 0.82 µg L^{-1}). Models using combined datasets showed lower accuracy, highlighting the importance of site-specific calibration. Wilcoxon signed-rank tests confirmed the absence of systematic bias between observed and predicted values. Ultimately, Sentinel-2 imagery combined with time-series cross-validation provides a reliable and cost-effective framework for the long-term monitoring of inland water quality.

Keywords: Alto Rabagão; Aguieira; chlorophyll-a; Secchi depth; eutrophication; empirical modelling; optical water quality

Check for updates

Academic Editor: Christos S. Akratos

Received: 7 June 2026
Revised: 27 June 2026
Accepted: 1 July 2026
Published: 7 July 2026

Copyright: © 2026 by the authors. Licensee MDPI, Basel, Switzerland. This article is an open access article distributed under the terms and conditions of the Creative Commons Attribution (CC BY) license.

1. Introduction

Population growth over recent decades has intensified anthropogenic pressures on natural resources, particularly freshwater systems [1]. Human activities, including intensive agriculture, industrialization, energy production, and urban supply, have significantly increased freshwater demand while simultaneously degrading water quality through the input of pollutants, excess nutrients, and organic matter [2]. This anthropogenic pressure does not occur in isolation: rather, it is intrinsically linked to global climate change. For example, greenhouse gas emissions from the same activities alter precipitation patterns, increase the frequency and intensity of extreme events (such as droughts and floods), and accelerate evaporation from water bodies [3]. As a consequence of this interconnectedness, many water bodies exhibit an energy imbalance between water use and natural replenishment, whereby extraction and evaporation losses exceed recharge capacity, exacerbating global water scarcity [2]. Projections indicate that by 2050, surface water deficit will affect 482 of the world's largest cities, reaching an estimated 6.75 million cubic meters due to the growing mismatch between water supply and demand [4].

Water scarcity is driven not only by reductions in water availability but also by deteriorating water quality [5,6]. Changes in hydrological conditions, such as prolonged droughts, altered precipitation regimes, and increased evaporation associated with climate change, can affect nutrient concentrations and biogeochemical processes within aquatic ecosystems. These changes frequently promote eutrophication, stimulate phytoplankton proliferation, increase turbidity, and reduce water transparency, thereby compromising ecosystem functioning and limiting water suitability for human consumption, agriculture, and industrial uses [2]. In this context, water quality has become a critical component of freshwater resource management, requiring continuous and reliable monitoring to support informed decision-making and ensure long-term ecosystem sustainability [7]. However, continuous assessment of water quality in aquatic ecosystems faces significant logistical and financial constraints. Traditional monitoring programs typically rely on periodic sampling campaigns, often conducted quarterly or semi-annually, which limit the detection of short-term events such as phytoplankton blooms, turbidity peaks, and rapid environmental fluctuations. Furthermore, these monitoring schemes may not adequately capture the spatial heterogeneity commonly observed within reservoirs. To overcome these limitations, remote sensing techniques have increasingly been integrated into water quality monitoring frameworks. Many studies have demonstrated strong relationships between field measurements and satellite-derived spectral information, enabling the development of empirical models that complement in situ observations while substantially enhancing temporal and spatial monitoring capabilities [7–9]. Despite these advantages, satellite-based monitoring is not without inherent limitations that can constrain its operational application. Key challenges include cloud contamination, which introduces significant data gaps, particularly during critical seasonal transition periods [10]. Furthermore, atmospheric correction remains a major source of uncertainty in optically complex inland waters [11]. Because the water-leaving radiance constitutes only a small fraction of the total signal recorded at the top of the atmosphere, minor errors in atmospheric correction, land adjacency effects, or sun glint (specular reflection) can propagate into substantial uncertainties in the estimation of water quality parameters like Chl-a and Secchi depth [10,11].

Remote sensing, using satellite or aerial imagery, enables continuous observation of lakes and reservoirs across large geographic areas, providing detailed information on water quality parameters, surface temperatures, and the upper water layer (approximately to the Secchi depth) [8]. These data can be acquired with high temporal frequency, often in near real-time, and in remote or otherwise inaccessible locations, providing an integrated and synoptic view of aquatic ecosystems dynamics that is difficult to achieve through

traditional monitoring methods alone [7]. The integration of remote sensing with advanced analytical techniques, such as machine learning models, further enhances its potential by improving the accuracy and robustness of water quality assessment [7]. In this context, the Sentinel-2 mission, integrated into the Copernicus European Program, is particularly relevant due to its high spatial resolution and short revisit time of approximately five days. The constellation of operational Sentinel-2 satellites (2A, 2B, and 2C) ensures consistent temporal coverage, making it particularly well-suited for monitoring the spatial and temporal dynamics of reservoir systems.

While other prominent satellite missions are widely used for environmental monitoring, Sentinel-2 offers a superior trade-off for small-to-medium inland water bodies when compared to Sentinel-3 and Landsat-8/9. For instance, although Sentinel-3 (OLCI) provides excellent spectral capabilities and daily revisits, its coarse spatial resolution (300 m) triggers severe land adjacency effects and mixed pixels in narrow or dendritic reservoir geometries. On the other hand, while Landsat-8/9 Operational Land Imager (OLI) features a suitable 30 m spatial resolution, it lacks the specialized red-edge spectral bands available in Sentinel-2 (at 20 m resolution) [12]. These red-edge bands are critical for capturing the specific reflectance peaks of chlorophyll-a, making Sentinel-2 uniquely suited for mapping the complex biogeochemical variations of these specific reservoir systems.

Over the last two decades, remote sensing has emerged as a key tool for monitoring inland water quality, due to its ability to provide synoptic, repetitive, and cost-effective observations over large spatial scales. Numerous studies have demonstrated the potential of multispectral satellite sensors to estimate key limnological variables, including chlorophyll-a (Chl-a), total suspended solids (TSS), turbidity, coloured dissolved organic matter (CDOM), Secchi disk depth (SD), and water surface temperature [9,12]. The increasing availability of free satellite imagery has further expanded the application of these techniques for operational water management and environmental monitoring. More recently, the integration of machine learning techniques has further enhanced remote sensing's capacity to retrieve limnological information. Algorithms such as Random Forest, Support Vector Machine, Artificial Neural Networks, and Extreme Gradient Boosting have shown superior predictive performance compared to traditional linear models, particularly in aquatic environments where nonlinear relationships between spectral responses and water quality variables are common [7,8]. However, these advanced algorithms typically require extensive datasets to avoid overfitting and often function as 'black boxes', which limits the direct physical interpretability of the spectral relationships. In scenarios constrained by the sample sizes typical of localized operational in situ networks, traditional empirical regression models remain a highly robust, parsimonious, and transparent alternative, allowing for a direct connection between specific band ratios and water quality parameters without introducing artificial complexity.

Despite these advancements, important challenges remain, particularly regarding the transferability of empirical models among reservoirs with different optical properties and hydrological regimes. Reservoirs with contrasting trophic conditions may exhibit markedly different spectral responses due to variations in phytoplankton biomass, suspended particles, coloured dissolved organic matter, and water transparency. Consequently, an important question is whether models developed from combined datasets can achieve predictive performance comparable to that of reservoir-specific models, or whether local calibration remains necessary for accurate water quality estimation. This highlights the need for region-specific calibration and validation procedures.

Within the Iberian Peninsula, several studies have explored these challenges. For instance, ref. [13] demonstrated the potential of Sentinel-2 Level-2A imagery for reservoir water quality monitoring, successfully estimating phycocyanin, SD, and TSS through em-

pirical models based on atmospherically corrected spectral indices. However, for Chl-a, no single model proved suitable across all reservoirs, requiring classification of water bodies into groups with distinct spectral characteristics. Although the proposed models were effective for spatiotemporal assessment, the authors highlighted the strong influence of local optical conditions on model performance. Beyond estimating water quality parameters, assessing their temporal evolution is essential for understanding whether aquatic ecosystems are undergoing long-term improvement or degradation. Trend analysis provides an objective framework for identifying persistent changes in water quality while distinguishing long-term signals from short-term fluctuations, thereby supporting environmental monitoring and water resource management [12]. Among the available approaches, the non-parametric Mann–Kendall (MK) test is widely used in hydrological and limnological studies because it detects monotonic trends without requiring normally distributed data or a predefined functional relationship [14]. In addition, its rank-based formulation makes it relatively insensitive to outliers, making it particularly suitable for environmental and remotely sensed water quality datasets [15]. Therefore, the MK test was adopted in this study to assess temporal trends in Sentinel-2-derived water quality parameters.

Given the above, this study aims to evaluate the temporal and spatial dynamics of water quality in two Portuguese reservoirs with contrasting trophic conditions, Alto Rabagão (Rb), an oligotrophic reservoir, and Aguieira (Ag), a eutrophic reservoir. Specifically, the study seeks to analyse temporal trends in Chl-a concentrations and water transparency, investigate the relationships between in situ measurements and Sentinel-2 Level-2A reflectance data, develop empirical models for estimating Chl-a and SD, and compare the performance of reservoir-specific and combined models to assess the transferability of remote sensing approaches across reservoirs with contrasting limnological conditions. Furthermore, spatial distribution maps derived from satellite imagery are produced to support reservoir monitoring and inform water resource management under changing environmental conditions.

2. Materials and Methods

2.1. Study Area

The study areas are located in Portugal, spanning two distinct hydrographic basins with contrasting geographic and environmental characteristics: the Cávado River basin in northern Portugal and the Mondego River basin in central Portugal (Figure 1). Within these basins, two major reservoirs were selected as the specific study areas: the Rb reservoir and the Ag reservoir, respectively. Both systems differ significantly in morphometry, hydrological regime, and watershed characteristics, allowing for the evaluation of distinct limnological and optical responses [16].

2.1.1. Alto Rabagão Reservoir

At the national and regional scale, the Rb reservoir is situated in the Vila Real district, northern Portugal, nested within the upper reaches of the Cávado River basin [17]. As the specific study area, it represents a regulated reservoir with morphometric and hydrological characteristics highly relevant to water quality studies. Identified in the national hydrometric network under code 03J/03A, the reservoir drains a catchment area of approximately 210 km^2. The region receives approximately 1500 mm of annual precipitation, resulting in a mean annual inflow of about 180,000 dam^3. Under extreme hydrological conditions, peak flood discharge can reach approximately 860 $m^3\ s^{-1}$. The key morphometric, operational, and limnological characteristics of the Rb reservoir, including its maximum storage capacity (568.69 hm^3) and water level operational limits, are summarized in Table 1.

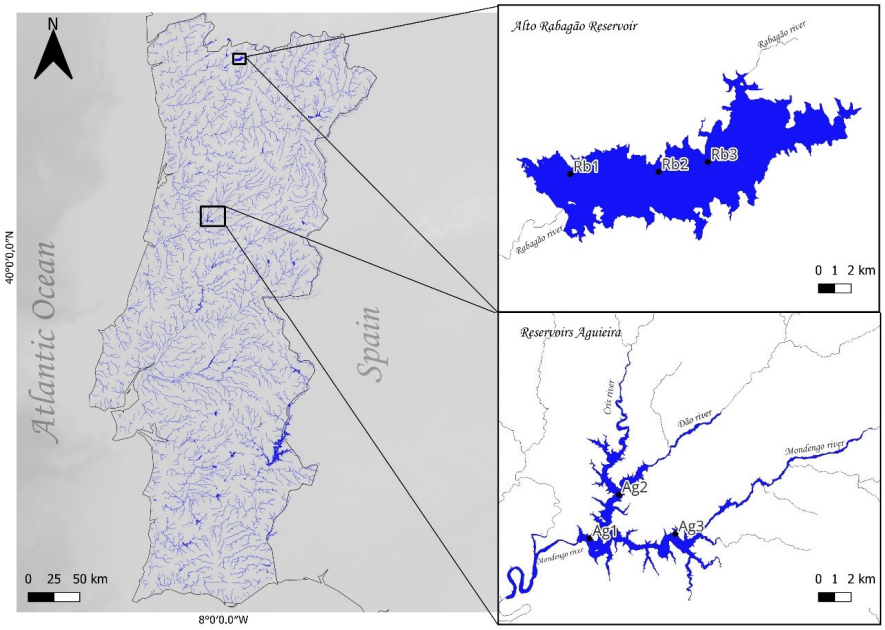


Figure 1. Location of the study areas and sampling sites in the Rabagão reservoir (Rb1—41°44′52.9″ N, 7°51′03.0″ W; Rb2—41°44′54.8″ N, 7°48′60.0″ W; and Rb3—41°45′04.9″ N, 7°47′51.4″ W) and in the Ag reservoir (Ag1—40°20′32.7″ N, 8°11′18.4″ W, Ag2—40°21′59.2″ N, 8°10′01.3″ W, and Ag3—40°20′41.6″ N, 8°07′34.0″ W).

Table 1. Morphometric, operational, and limnological characteristics of the Alto Rabagão (Rb) and Aguieira (Ag) reservoirs.

Parameter	Rb	Ag
Location/Region	Vila Real, Northern Portugal	Coimbra/Viseu, Central Portugal
River Basin	Cávado River basin	Mondego River basin
Surface Area ($km^{2)}$	22.12	20
Maximum Volume (hm^3)	568.69	423
Maximum Depth (m)	94	89
Mean Depth (m)	25.7	21.1
Trophic State	Oligo-mesotrophic	Eutrophic
Primary Water Use	Hydropower generation, irrigation and water supply	Hydropower generation, irrigation and water supply
Surrounding Land Use	Undeveloped lands, agriculture, pastures and forests	Forests, agriculture and artificial territories

2.1.2. Aguieira Reservoir

Further south, the Ag reservoir is located in central Portugal, positioned between the districts of Coimbra and Viseu. The reservoir is situated along the middle stretch of the Mondego River basin, near the river's confluence with the Dão and Cris rivers (Figure 1). As a core study area built in 1981, the reservoir covers approximately 20 km^2 and is primarily used for hydroelectric power generation, irrigation, and water storage. The regional climate is Mediterranean, characterized by mild to cold winters and hot, dry summers. Limnologically, the reservoir behaves as a warm monomictic system, exhibiting thermal stratification during the warmer months and complete mixing during winter. Water levels exhibit marked seasonal fluctuations, ranging from 126 m to 110 m, corresponding to substantial variations in storage capacity. The environmental and morphometric parameters of the Ag reservoir are contrasted with those of the Rb reservoir in Table 1, highlighting their divergent hydrological regimes, primary water uses (such as hydropower and human consumption), and surrounding land use influences. The surrounding catchment area is influenced by mixed land use, including forested areas, agriculture, and industrial activities, which may affect the reservoir's limnological dynamics [17].

Unlike more isolated systems, the presence of populated urban centers and industrial facilities within the Mondego river basin subjects the Ag reservoir to complex anthropogenic pressures. Consequently, the system experiences continuous and significant nutrient enrichment (particularly phosphorus and nitrogen) [17]. This loading is driven simultaneously by diffuse pollution, such as agricultural and urban surface runoff during rainfall events, and by point-source pollution, including domestic wastewater discharges. Driven by this continuous influx of nutrients, the Ag reservoir is limnologically classified as a eutrophic system (occasionally shifting to mesoeutrophic during periods of high river inflow). Environmentally, this results in high phytoplankton biomass, frequently elevated Chl-a concentrations, reduced water transparency, and a known susceptibility to seasonal cyanobacterial blooms.

2.2. Limnological Data

Data were obtained from two complementary sources: (i) official monitoring stations operated by the Portuguese Environment Agency (APA/SNIRH) and (ii) in situ sampling campaigns conducted directly by our research group. The official network included two stations at the Rb reservoir—Station 1 int CCHE (code 03J/17C; 41°44′31″ N, 7°51′11″ W) and Station 2 int CCHE (code 03J/13C; 41°44′28″ N, 7°50′27″ W) and two stations at the Ag reservoir, namely Station 1 (code 11H/11C; 40°20′37.39″ N, 8°11′38.69″ W) and Station 2 (code 11H/11M; 40°20′14.78″ N, 8°11′03.98″ W). Complementing these official data, our research group's field campaigns covered three dedicated sampling sites at Rb (Rb1, Rb2, Rb3) and three at Ag (Ag1, Ag2, Ag3) (Figure 1). Across both data sources, the primary parameters analysed were water transparency and Chl-a concentration (μg L^{-1}). Chl-a was determined spectrophotometrically after pigment extraction with 90% acetone, following the standard protocol defined by Lorenzen (1967) [18]. Water transparency was evaluated in the field using a standard 30 cm diameter black-and-white SD (m). To ensure accuracy and minimize errors from solar glare, SD measurements were performed on the shaded side of the vessel by lowering the disk until it disappeared from sight, recording the depth, and subsequently averaging it with the depth of reappearance.

Each reservoir was originally sampled at three monitoring locations (Figure 1). However, to ensure consistency with the official monitoring strategy adopted by the Portuguese Environment Agency (APA), which typically prioritizes the station located near the dam outlet, only data from the first sampling site (Rb1, Ag1) were used in this study. This location was selected because it best represents the operational monitoring station commonly used for water quality assessment and long-term surveillance of inland reservoirs. From a limnological and optical perspective, focusing on this deeper, lacustrine zone near the dam infrastructure is methodologically sound, as it represents the largest, most stable water volume and serves as a reliable indicator of the reservoir's overall trophic state. Furthermore, for satellite remote sensing applications, selecting these deeper central areas minimizes potential bottom-reflectance contamination and the localized turbidity gradients typical of shallower upstream riverine transitions, thereby reducing spatial noise during model development. Consequently, all spectral indices, model calibration, and statistical analyses were performed exclusively using observations from this sampling site (Rb1, Ag1). No spatial averaging across the three sampling locations within each reservoir was applied.

The APA/SNIRH monitoring program provided bimonthly measurements collected at the official monitoring stations between 2014 and 2024. Complementarily, the research group conducted seasonal field campaigns in 2023 and 2024, with four sampling surveys per year representing winter, spring, summer, and autumn conditions at the three sampling locations. The integration of long-term monitoring data with high-frequency seasonal observations enabled a comprehensive assessment of both temporal variability and seasonal

dynamics of water quality parameters in the reservoir. To ensure data comparability and eliminate analytical bias, both data sources relied on identical, standardized methodologies: water transparency was consistently measured using standard white-and-black SD, and Chl-a concentrations from both the official monitoring program and field campaigns were determined spectrophotometrically following equivalent pigment extraction protocols by Lorenzen [18].

Before analysis, the dataset underwent quality control procedures. Outliers were identified using the interquartile range (IQR) method proposed by Tukey [19] and further evaluated by visual inspection with boxplots. Extreme values were removed only when associated with measurement inconsistencies or clearly non-representative conditions, thereby preserving the dataset's natural variability. Through this procedure, a total of 5 observations from the Rb reservoir and 3 observations from the Ag reservoir were identified as anomalous outliers and removed from the baseline database. These extreme values were linked to localized field sampling anomalies or minor laboratory measurement inconsistencies. Removing these few anomalous data points prevented artificial skewness in the subsequent statistical analyses and model calibrations, ensuring that the dataset accurately reflects the true, representative limnological and seasonal dynamics of both water bodies.

2.3. Temporal Trend Analysis

Temporal trends were evaluated using both parametric and non-parametric approaches. Simple linear regression, based on ordinary least squares (OLS), was applied to estimate the magnitude and direction of temporal trends (slope coefficient, β), following the framework described by Draper [20]. Model assumptions, including normality and homoscedasticity of residuals, were assessed through visual inspection of residual plots.

To complement this analysis and account for non-normal data distributions and the presence of outliers, the non-parametric Mann–Kendall (MK) test was applied to detect monotonic trends at a 95% confidence interval ($\alpha = 0.05$) [14,15]. The MK test evaluates the null hypothesis (H_0) of no trend against the alternative hypothesis (H_1) of a monotonic increasing or decreasing trend. The MK test statistic S is calculated as follows:

$$S = \sum_{i=1}^{n-1} \sum_{j=i+1}^{n} sgn(x_j - x_i) \quad (1)$$

where x_i and x_j represent the sequential data values at times i and j (j > i), n is the total number of data points, and $sgn(x_j - x_i)$ is the sign function defined as:

$$sgn(x_j - x_i) = \begin{cases} +1, & if\ x_j - x_i > 0 \\ 0, & if\ x_j - x_i = 0 \\ -1, & if\ x_j - x_i < 0 \end{cases} \quad (2)$$

For datasets with $n \geq 10$, a standard normal test statistic Z_{MK} is computed to test the significance of the trend, using the variance of S (Var(S)) corrected for tied groups:

$$Z_{MK} = \begin{cases} \frac{S-1}{\sqrt{Var(S)}}, & if\ S > 0 \\ 0, & if\ S = 0 \\ \frac{S+1}{\sqrt{Var(S)}}, & if\ S < 0 \end{cases} \quad (3)$$

A positive value of Z_{MK} indicates an increasing monotonic trend, whereas a negative value indicates a decreasing trend. The null hypothesis of no trend is rejected if $|Z_{MK}| > Z_1 - \frac{\alpha}{2}$ where $Z_1 - \frac{\alpha}{2}$ is the standard normal deviates at the chosen significance level ($\alpha = 0.05$).

Additionally, autocorrelation in the time series was evaluated using the Durbin–Watson statistic [21], ensuring that the residuals were independent. Descriptive statistics, including mean, minimum, maximum, median, standard deviation, and coefficient of variation, were calculated to characterize the dataset's variability.

2.4. Sentinel-2 Data Acquisition and Processing

Sentinel-2 Level-2A (surface reflectance) images were obtained from the Copernicus Browser platform. Image selection followed strict criteria, including a maximum temporal difference of ±3 days relative to in situ sampling dates, cloud cover below 30%, and the absence of visible atmospheric artifacts over the reservoir.

For each reservoir, a Region of Interest (ROI) of approximately 0.008 km^2 was defined to encompass the in situ sampling locations. This ROI size was selected to ensure spatial representativeness while minimizing edge effects such as land–water spectral mixing, as recommended in remote sensing studies of inland waters [12]. At a spatial resolution of 10 m, this area corresponds to 80 pixels. The selection of this specific ROI dimension was further supported by a preliminary sensitivity analysis testing various window sizes (including single-pixel extraction, 3 × 3, and 5 × 5-pixel matrices). Smaller pixel windows exhibited higher vulnerability to instrumental noise and spatial mismatch caused by the boat's drift and GPS positioning uncertainty (± 3–5 m) during field sampling. Conversely, larger windows increased the risk of spectral contamination from shoreline adjacency effects. Thus, the 0.008 km^2 ROI provided the optimal trade-off, maximizing the signal-to-noise ratio while ensuring strict spatial correspondence with the physical samples. Mean reflectance values were extracted for each spectral band within the ROI.

2.5. Spectral Indices and Empirical Modelling

Several spectral indices commonly used in inland-water remote sensing were evaluated for estimating Chl-a concentration and SD. For Chl-a, the tested indices included the Dall'Olmo [22] three-band index (TBDO) [13,23], the Maximum Chlorophyll Index (MCI) [13], the Normalized Difference Index (NDI), and simple band ratios (SR). The selection of band combinations was based on Sentinel-2 spectral bands, specifically the blue (490 nm), green (560 nm), red (665 nm), and red-edge bands (705 and 740 nm), which are known to be sensitive to variations in phytoplankton biomass and optical water properties.

The general formulations of the evaluated indices are:

$$NDI = \frac{R_i - R_j}{R_i + R_j} \quad (4)$$

$$TBDO = R_i \cdot \left(\frac{1}{R_j} - \frac{1}{R_k}\right) \quad (5)$$

$$MCI = R_i - \alpha \cdot \left(R_j + (R_k - R_k) \cdot \beta\right) \quad (6)$$

NDI = Normalized difference index
Ri, j = reflectivity in bands i, j
TBDO = Dall'Olmo Triband Index
MCI = MERIS Maximum Chlorophyll Index
α, β = adjustment parameters

For Chl-a estimation, several spectral combinations derived from the Sentinel-2 visible and red-edge bands were evaluated. The three-band Dall'Olmo index was implemented in two configurations: TBDO1, defined as R665(1/R560 − 1/R443), and TBDO, defined as R740(1/R665 − 1/R705) [17], both designed to enhance sensitivity to phytoplankton absorption features.

The MCI, which exploits the spectral peak associated with chlorophyll fluorescence, was also tested, together with normalized difference indices (NDI), computed as (R560 − R490)/(R560 + R490), which capture relative differences between green and blue reflectance. The Normalized Difference Vegetation Index (NDVI), expressed as (R560 − R665)/(R560 + R665), was included as a proxy for pigment-related absorption in inland waters.

In addition, the Chlorophyll Index (CI), based on inverse reflectance relationships between green and red bands, and simple band ratios such as Green/Red = R560/R665 and Blue/Red = R490/R665 were evaluated to capture variations in water colour associated with phytoplankton concentration.

For water transparency (SD), normalized difference indices and simple band ratios related to water colour and light attenuation were evaluated, including Green/Red, Blue/Red, and Green/Blue combinations.

The relationship between field measurements and spectral indices was modelled using multiple regression formulations, including linear, second- and third-order polynomial, logarithmic, exponential, reciprocal, square-root, and power models [24]. Model parameters were estimated using least-squares regression. Model performance was evaluated using the coefficient of determination (R^2) and root mean square error (RMSE) [25]. The best-performing models were selected based on their predictive accuracy while considering model simplicity and avoiding unnecessary complexity [26].

2.6. Time-Series Cross-Validation (Walk-Forward)

To ensure the robustness of the models under temporal dependency, a walk-forward validation approach (time-series cross-validation) was implemented, following the methodology described by Hyndman [26]. This approach preserves the data's chronological order and prevents information leakage between the training and test sets.

The procedure consisted of an initial training phase using approximately 40% of the earliest observations, followed by sequential prediction of subsequent observations. After each prediction, the model was updated by adding the new data point to the training set, enabling iterative recalibration [27].

2.7. Performance Metrics

Model predictive performance and statistical accuracy during both calibration and walk-forward time-series cross-validation phases were comprehensively evaluated using a complementary suite of standard performance metrics. These included the cross-validated Coefficient of Determination (R^2cv), Root Mean Square Error (RMSE), Mean Absolute Error (MAE), and Mean Absolute Percentage Error (MAPE) [25,26]. The mathematical formulations and structural definitions of these metrics are defined as follows:

The R^2 measures the proportion of variance in the in situ observed water quality data that is predictable from the satellite-derived spectral indices. It provides a standardized measure of goodness-of-fit ranging from 0 to 1, where higher values indicate stronger explanatory power under model validation conditions:

$$R^2 = 1 - \frac{\sum_{i=1}^{n}(y_i - \hat{y}_i)^2}{\sum_{1=1}^{n}(y_i - \overline{y})^2} \quad (7)$$

The RMSE quantifies the overall magnitude of the prediction error by calculating the square root of the mean squared differences between satellite-modelled estimates and in situ field observations. Because it squares the errors before averaging, RMSE penalizes larger

errors and outliers more heavily, making it a critical diagnostic indicator for water-quality retrieval variances under shifting optical conditions:

$$RMSE = \sqrt{\frac{1}{n}\sum_{i=1}^{n}(y_i - \hat{y}_i)^2} \quad (8)$$

The MAE provides a robust, linear measure of the average absolute deviation between the predicted values and actual field observations. Unlike RMSE, MAE treats all individual differences equally and is less sensitive to extreme outliers, offering an unweighted assessment of typical model error magnitude in long-term environmental monitoring datasets:

$$MAE = \frac{1}{n}\sum_{i=1}^{n}|y_i - \hat{y}_i| \quad (9)$$

The MAPE assesses the relative percentage accuracy of the empirical predictions against the scale of the observed baseline values. This metric is highly valuable for cross-comparing model performance across different systems, as it contextualizes the absolute error relative to the magnitude of the measured parameter (e.g., assessing a specific error margin in low-biomass vs high-biomass environments).

$$MAPE = \frac{1}{n}\sum_{i=1}^{n}\frac{|y_i - \hat{y}_i|}{|y_i|} \times 100\% \quad (10)$$

where y_i represents the i-th in situ observed value (Chl-a or SD), $\hat{y}$ is the corresponding satellite-predicted value, $\overline{y}$ is the mean of the observed values, and n denotes the total number of paired observations in the validation subset. Lower absolute values for RMSE, MAE, and MAPE indicate enhanced predictive stability and accuracy, while values approaching unity for R^2cv demonstrate robust model performance and reliable transferability under operational conditions. The statistical significance of the fitted validation regressions was evaluated using *p*-values based on an established significance threshold of $p < 0.05$ [25,26].

2.8. Statistical Validation of Empirical Models

To further assess the reliability of the empirical models for Chl-a and SD, modelled values were statistically compared with their corresponding in situ observations using paired analyses. Initially, the normality of the paired differences was evaluated using the Shapiro–Wilk test [28]. When normality assumptions were satisfied, paired Student's *t*-tests were applied. Otherwise, the non-parametric Wilcoxon signed-rank test was used.

These analyses were performed to verify whether statistically significant differences existed between modelled and observed datasets and to identify potential systematic biases in model predictions. All statistical analyses were conducted in the R environment [29].

2.9. Spatial Distribution Mapping

Spatial distribution maps of Chl-a and SD were generated by applying the validated empirical models to Sentinel-2 Level-2A surface reflectance imagery obtained from the Copernicus Browser platform. After model validation, the regression equations were implemented in the platform's Custom Script tool using JavaScript-based Evalscript routines. The scripts enabled the pixel-by-pixel application of the empirical models across the reservoir surface, allowing the spatial estimation of water quality parameters. To improve map quality and eliminate land-surface noise, shoreline mixed pixels, and edge artifacts, a stringent water masking procedure was implemented prior to model execution. The Normalized Difference Water Index (NDWI) [30] was incorporated into the Evalscript routine to delineate open water surfaces, capitalizing on the contrast between the Green (Band

3—560 nm (B3)) and Near-Infrared (NIR, Band 8—842 nm(B8)) channels of the Sentinel-2 Multispectral Instrument (MSI) as follows:

$$NDWI = \frac{B3 - B8}{B3 + B8} \quad (11)$$

To ensure high data quality and avoid terrestrial pixel contamination along the irregular margins of the reservoirs, a strict conservative threshold condition was enforced. Pixels were processed for empirical parameter estimation only if they met the condition NDWI ≥ 0.15 alongside valid operational data masking (dataMask $\neq 0$). Pixels failing these criteria were strictly discarded and assigned null output values [0,0,0,0]. Only atmospherically corrected images with low cloud cover and adequate visual quality were selected. Representative dates were chosen to illustrate seasonal patterns and temporal variations in optical water properties. All image processing, model implementation, spatial analyses, and map generation procedures were performed using the R (version 4.5.2) environment and the Copernicus Browser platform.

3. Results

3.1. Descriptive Statistics

Descriptive statistics revealed clear differences in the limnological behavior of the two reservoirs over the study period (2014–2024) (Table 2). The Rb exhibited lower mean Chl-a concentrations (5.25 μg L^{-1}) compared to the Ag (10.8 μg L^{-1}), indicating lower average phytoplankton biomass. Despite this difference, both systems showed high temporal variability, with Chl-a coefficients of variation exceeding 99%.

Table 2. Descriptive statistics, linear regression, and Mann–Kendall trend analysis results for limnological parameters in the Rb and Ag reservoirs (2014–2024).

	Parameters	Chl-a (μg L^{-1})	SD (m)
Rb	n (samples)	118	80
	Mean	5.25	4.18
	Minimum	0.32	0.50
	Maximum	32.0	7.40
	Median	3.62	4.40
	Standard Deviation	5.22	1.51
	Coefficient of Variation	99.3	35.5
	Skewness	2.86	−0.255
	Kurtosis	12.6	2.71
	Z_{MK}	+3.20	−3.98
	MK *p*-value	$p < 0.01$	$p < 0.001$
Ag	n (samples)	81.0	75.0
	Mean	10.8	2.83
	Minimum	0.97	0.70
	Maximum	62.5	5.50
	Median	7.40	3.00
	Standard Deviation	11.6	1.09
	Coefficient of Variation	107	38.6
	Skewness	2.45	0.025
	Kurtosis	10	2.35
	Z_{MK}	+0.16	−0.79
	MK *p*-value	0.870	0.428

Water transparency was consistently higher in Rb (mean = 4.18 m) than in Ag (2.83 m), indicating clearer water in Rb. Temporal variability in SD depth was also observed in both reservoirs, reflecting seasonal and interannual fluctuations in water optical conditions.

3.2. Temporal Trends

Rb and Ag

The temporal evolution of limnological parameters in the Rb and Ag reservoirs is presented in Figure 2 and further detailed in the integrated statistical analysis (Table 2). For Rb, Chl-a exhibited a statistically significant increasing trend (Figure 2a), with a parametric slope of $\beta = 1.038 \times 10^{3}$ µg L^{-1} day $^{-1}$($p = 0.0159$), corresponding to an annual increase of approximately 0.38 µg L^{-1}. This upward trajectory was robustly supported by the non-parametric Mann–Kendall test, which yielded a significant positive standard statistic ($Z_{MK} = +3.20$, $p = 0.0014$). In contrast, SD in Rb showed a significant decreasing trend (Figure 2c), indicating a progressive reduction in water transparency ($\beta = -6.015 \times 10^{-4}$ m day^{-1}; $p < 0.001$), a pattern strongly corroborated by a highly significant negative Mann–Kendall statistic ($Z_{MK} = -3.98$, $p < 0.001$).

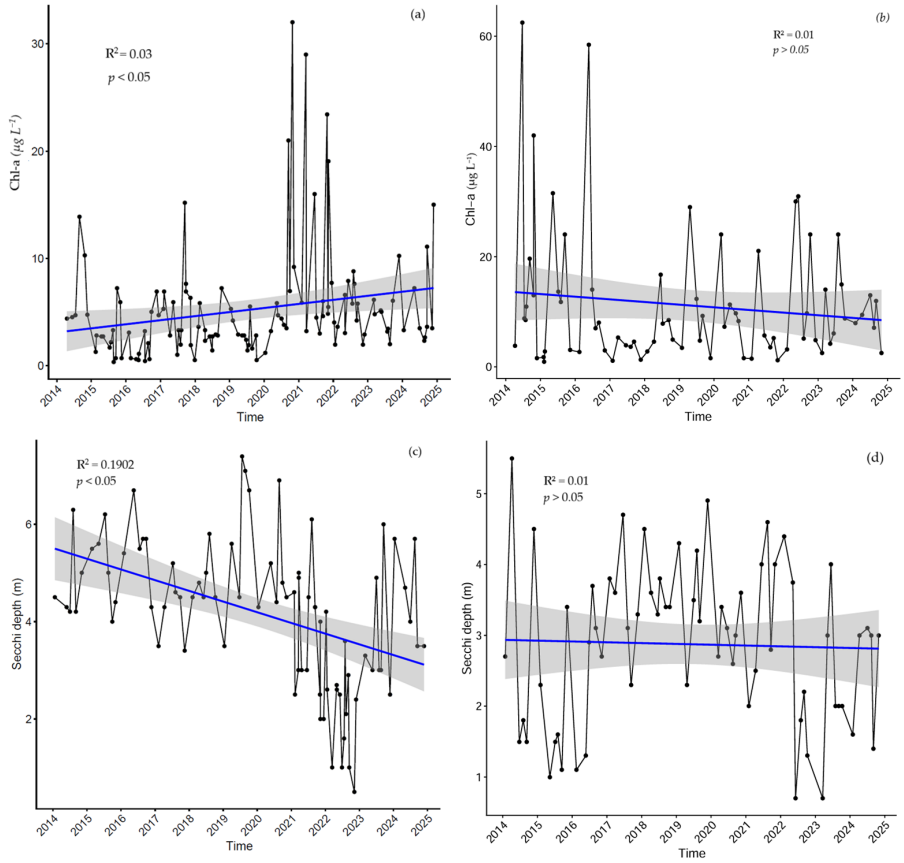


Figure 2. Rb and Ag temporal evolution and interannual variability of Chl-a: (**a**)—Rb, (**b**)—Ag (µg L^{-1}), SD: (**c**)—Rb, (**d**)—Ag (m), from 2014 to 2024. Panels include linear regression fit with 95% confidence interval.

Together, these convergent results demonstrate a robust, coupled ecological shift in this oligotrophic system, where rising phytoplankton biomass directly drives the decline in water clarity. Regarding Ag, the parameters displayed a completely different behavior characterized by stability. Chl-a showed high interannual variability (Figure 2b), but no statistically significant trend was recorded by the linear regression ($\beta = -1.426 \times 10^{-3}$ µg L^{-1} day $^{-1}$, $p = 0.168$; $R^2 = 0.011$) or the non-parametric Mann–Kendall test, which resulted in a near-zero standard statistic ($Z_{MK} = +0.16$, $p = 0.870$).

Similarly, SD remained stable over time (Figure 2d), with no significant long-term trends observed in either the linear model ($\beta = -6.41 \times 10^{-5}$ m day^{-1}, $p = 0.541$; $R^2 = 0.005$) or the non-parametric approach ($Z_{MK} = -0.79$, $p = 0.428$). These findings indicate that while the oligotrophic Rb reservoir is undergoing directional environmental shifts, the eutrophic Ag reservoir maintains a steady-state baseline dominated by cyclical variations rather than a multi-year trajectory.

3.3. Relationships Between Limnological Variables

The relationships between Chl-a and water transparency are shown in Figure 3. In the Rb reservoir, Chl-a showed a moderate negative relationship with SD (Figure 3a; $SD = 6.211 * Chl - a^{(-0.248)}$, indicating that increases in phytoplankton biomass reduced water transparency. In the Ag reservoir, Chl-a also showed a negative relationship with SD (Figure 3b; $SD = 4.425 * Chl - a^{(-0.234)}$,). For the combined dataset, a moderate negative relationship was observed between Chl-a and SD (Figure 3c; $SD = 5.95 * Chl - a^{(-0.32)}$).

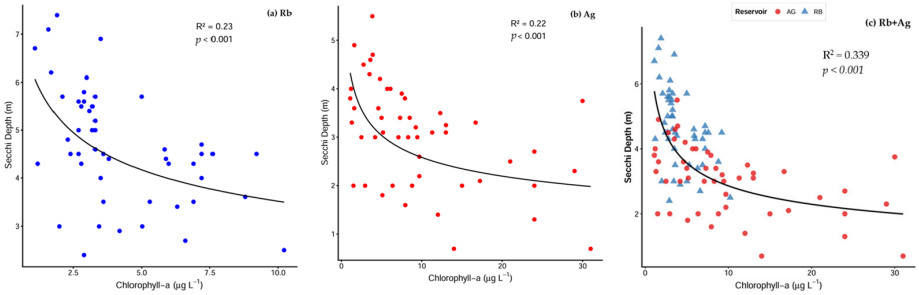


Figure 3. Relationships between Chl-a, and SD in the studied reservoirs. (**a**) SD vs. Chl-a in Rb; (**b**) SD vs. Chl-a in Ag; (**c**) SD vs. Chl-a in Rb + Ag.

3.4. Performance of Sentinel-2 Empirical Models: Reservoir-Specific Models

In the Rb reservoir, the best model for Chl-a estimation was based on the TBDO1 index, with an exponential formulation reaching $R^2 = 0.637$. SD was best estimated using the NDI ratio (Table 3), with $R^2 = 0.503$.

Table 3. Performance of empirical models for estimating limnological parameters from spectral indices (Sentinel-2 L2A) in the Rb and Ag. Regression: linear (L); Exponential (exp), Potential (pot); logarithmic (log).

	Parameter	Index	Bands Relation	Order	n	R^2
Rb	**Chl-a**	**TDBO1**	**R665(1/R560 − 1/R443)**	**Exp**	**23**	**0.637**
		B2/B4	R490/R665	Exp	23	0.580
		TDBO1	R665(1/R560 − 1/R443)	L	23	0.565
		B2/B4	R490/R665	L	23	0.479
		B2/B4	R490/R665	Pot	23	0.465
	SD	**NDI**	**(R560 − R665)/(R560 + R665)**	**L**	**24**	**0.503**
		B2/B4	R490/R665	Exp	24	0.472
		NDI	(R560 − R665)/(R560 + R665)	Exp	24	0.461
		B3/B4	R560/R665	Exp	24	0.413
Ag	**Chl-a**	**TBDO**	**R740(1/R665 − 1/R705)**	**Exp**	**21**	**0.748**
		TBDO	R740(1/R665 − 1/R705)	L	21	0.635
		TDBO1	R665(1/R560 − 1/R443)	L	21	0.210
	SD	**MCI**	**R560 − 0.4031R665 − 0.6359R490**	**Exp**	**25**	**0.551**
		MCI	R560 − 0.4031R665 − 0.6359R490	L	25	0.539
Rb + Ag	**Chl-a**	**TDBO1**	**R665(1/R560 − 1/R443)**	**Exp**	**41**	**0.635**
		TDBO1	R665(1/R560 − 1/R443)	L	41	0.455
		MCI	R665 + 11.177R560 − 13.274R490	Exp	41	0.305
	SD	**MCI**	**R560 − 0.4031R665 − 0.6359R490**	**Exp**	**51**	**0.503**
		MCI	R560 − 0.4031R665 − 0.6359R490	L	51	0.478
		NDI	(R560 − R665)/(R560 + R665)	Exp	51	0.281

In the Ag reservoir, model performance was generally higher. The TBDO index provided the best estimates for Chl-a (R^2 = 0.748). SD was best estimated using the MCI index (R^2 = 0.551; Table 3).

When both reservoirs were combined, the model's performance decreased (Table 3). The Chl-a estimate maintained moderate performance (R^2 = 0.635) in the TBDO1 index, and the SD also showed predictive power ($R^2 \approx 0.503$) using the MCI index.

3.5. Model Calibration and Validation

Model performance was evaluated using a time-series cross-validation approach (walk-forward validation), which is specifically designed for temporally ordered environmental datasets. In this method, models are iteratively trained on past observations and tested on subsequent unseen observations, preserving the temporal structure of the data and avoiding random data splitting.

Performance results were summarized in Table 4 and illustrated in Figure 4. The left panels (a, c, e, g) show the calibration results, while the corresponding right panels (b, d, f, h) present the walk-forward validation results for each model. For the Rb reservoir, the best-performing model for Chl-a, based on the TBDO1 index, achieved a cross-validated coefficient of determination of R^2cv = 0.67, with RMSE = 1.10 µg L^{-1}, MAE = 0.82 µg L^{-1}, and MAPE = 26.8% (Table 4; Figure 4a,b). In contrast, the SD model for Rb showed lower predictive performance, with R^2cv = 0.26.

Table 4. Time-series cross-validation performance of empirical models for estimating limnological parameters using Sentinel-2 data. * Best models.

	Model	R^2_{cv}	RMSE	MAE	MAPE (%)	*p*-Value	n_{cv}
Rb	$Chl-a\left(\mu gL^{-1}\right) = 1.888 \cdot e^{(-1.1323 \cdot TDBO1)}$	0.67 *	1.10	0.82	26.8	$p = 0.002$	14
	$SD(\mathrm{m}) = 5.568 - 3.542 \cdot NDI$	0.26	1.29	1.07	44.4	$p < 0.001$	15
Ag	$Chl-a\left(\mu gL^{-1}\right) = 7.745 \cdot e^{(6.2408 \cdot TBDO2)}$	0.68 *	3.60	2.92	31.2	$p < 0.001$	13
	$SD(\mathrm{m}) = 4.295 \cdot e^{(-42.467 \cdot MCI)}$	0.49 *	0.61	0.50	17.2	$p < 0.001$	15
Rb + Ag	$Chl-a\left(\mu gL^{-1}\right) = 2.466 \cdot e^{(-0.9194 \cdot TBDO1)}$	0.37	4.22	2.34	47.1	$p < 0.001$	36
	$SD(\mathrm{m}) = 4.446 \cdot e^{(-45.8029 \cdot MCI)}$	0.45 *	0.89	0.71	23.7	$p < 0.001$	46

For the Ag reservoir, the best Chl-a model (TBDO) achieved R^2cv = 0.68, with RMSE = 3.6 µg L^{-1}, MAE = 2.92 µg L^{-1}, and MAPE = 31.2% (Table 4; Figure 4c,d). The SD model for Ag, based on the MCI index, showed moderate performance (R^2cv = 0.49; Figure 4e,f). For the combined dataset (Rb + Ag), model performance for SD decreased, with a maximum R^2cv of 0.45 (Table 4; Figure 4g,h).

The comparison between calibration and cross-validated performance revealed no evidence of substantial overfitting. For Chl-a models, the differences between R^2 and R^2cv were small: Rb (+0.033) and Ag (−0.068). Similarly, for Secchi depth models, the differences were also limited: Ag (−0.061). The close agreement between calibration and validation metrics indicates that the models capture generalizable relationships rather than noise specific to the training data, supporting their temporal robustness.

Overall, visual inspection of Figure 4 indicates that Chl-a models (panels a–d) exhibit closer agreement between observed and predicted values, with data points distributed more closely around the 1:1 line (dashed red). In contrast, SD models (panels e–h) show greater dispersion and reduced predictive stability, particularly for the Rb reservoir and the combined dataset.

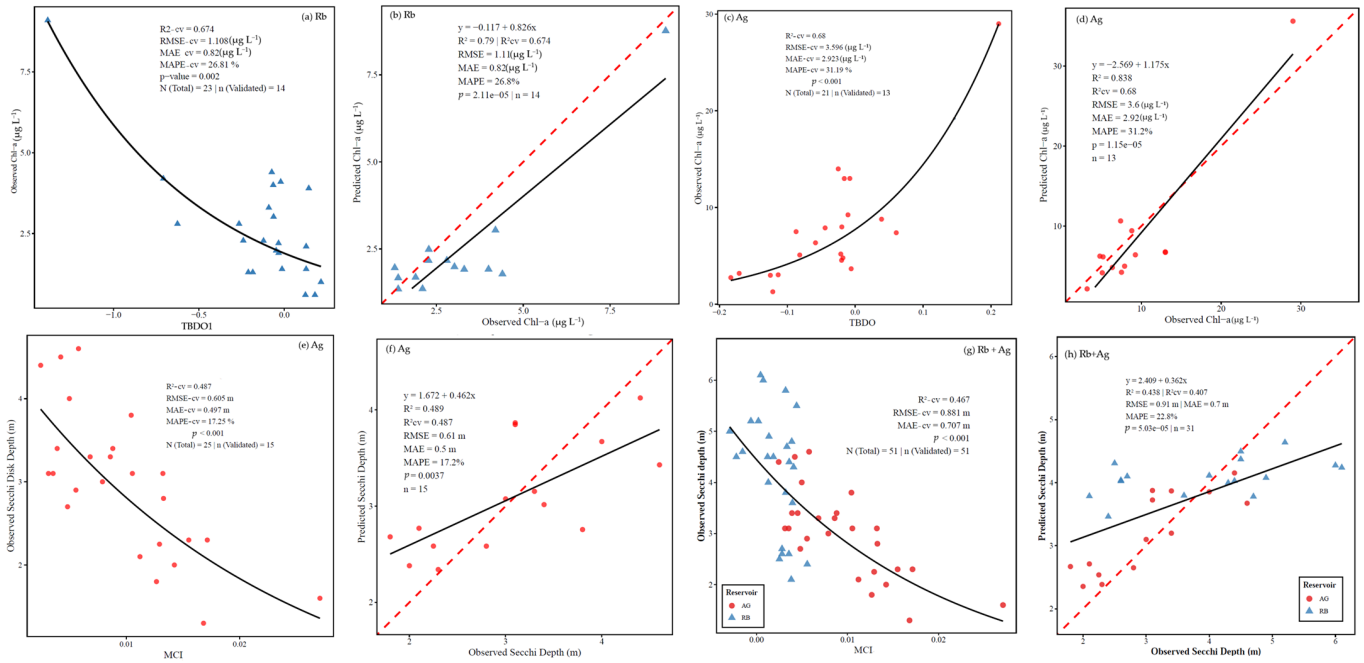


Figure 4. Observed vs. predicted values of Chl-a and SD based on the best validated empirical models (time-series cross-validation). Panels show: (**a**) Chl-a vs. TBDO1 in Rb; (**c**) Chl-a vs. TBDO in Ag; (**e**) SD vs. MCI in Ag; and (**g**) SD vs. MCI using combined data from both reservoirs. The respective validation panels are shown in (**b**,**d**,**f**,**h**). In the validation panels (**b**,**d**,**f**,**h**), the solid black line represents the fitted linear regression, and the dashed red line indicates the 1:1 relationship between observed and predicted values.

3.6. Statistical Validation of Modelled and Observed Data

The statistical validation demonstrated strong agreement between modelled and in situ observations for both Chl-a and SD in the studied reservoirs. For Chl-a in the Rb reservoir, the Shapiro–Wilk test indicated non-normal distribution of paired differences ($W = 0.900$; $p = 0.026$). Consequently, validation was performed using the Wilcoxon signed-rank test, which revealed no statistically significant differences between modelled and observed values ($V = 163$; $p = 0.463$).

In the Ag reservoir, paired differences followed a normal distribution ($W = 0.964$; $p = 0.603$), allowing the application of the paired *t*-test, which also showed no statistically significant differences between observed and modelled Chl-a values ($t = 0.997$; d.f. = 20; $p = 0.331$). For Secchi disk depth, paired differences were normally distributed in both reservoirs (Rb: $W = 0.956$, $p = 0.273$; Ag: $W = 0.952$, $p = 0.253$). Paired *t*-tests indicated no statistically significant differences between modelled and observed transparency values in either reservoir (Rb: $t = -0.934$, d.f. = 27, $p = 0.358$; Ag: $t = 0.938$, d.f. = 25, $p = 0.357$).

Overall, these results confirm that the empirical models reproduced the temporal variability of Chl-a and water transparency without significant systematic bias, reinforcing the robustness of the proposed Sentinel-2-based approach for reservoir water-quality monitoring.

3.7. Spatial Distribution of Chl-a and Secchi Depth

The spatial distribution maps of Chl-a and SD revealed clear heterogeneity in water quality conditions across both reservoirs. In the Rb reservoir (Figure 5), higher Chl-a concentrations were predominantly observed in localized zones, particularly in upstream and nearshore areas, while lower values were generally associated with open-water regions.

A consistent inverse spatial pattern was observed for Secchi depth, with higher water transparency in areas with lower phytoplankton biomass.

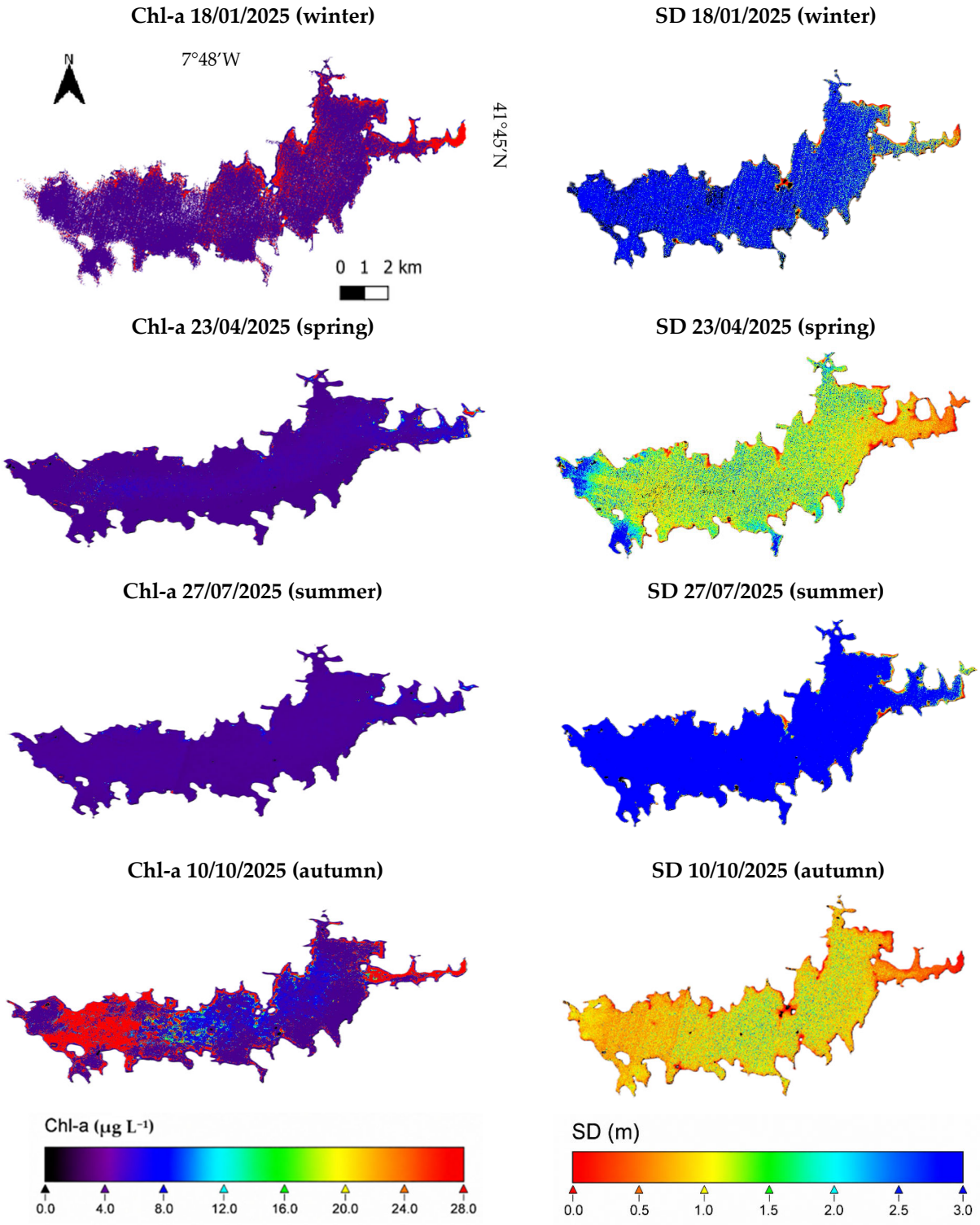


Figure 5. Spatial distribution maps of Chl-a and SD in the Rb Reservoir derived from Sentinel-2 L2A imagery, across different seasons in 2025.

In the Ag reservoir (Figure 6), spatial patterns were more variable, with elevated Chl-a concentrations distributed across broader areas of the reservoir surface. SD showed a corresponding reduction in water transparency in these areas, although spatial gradients were less stable than those of Rb, indicating more dynamic optical conditions. Tempo-

ral analysis of selected dates indicated seasonal shifts in the spatial distribution of both parameters. Periods of increased Chl-a concentrations generally coincided with reduced Secchi depth, reinforcing the inverse relationship between phytoplankton biomass and water transparency. Overall, the spatial maps highlight distinct heterogeneity patterns between the reservoirs: Rb shows more structured spatial gradients, whereas Ag shows greater temporal and spatial variability.

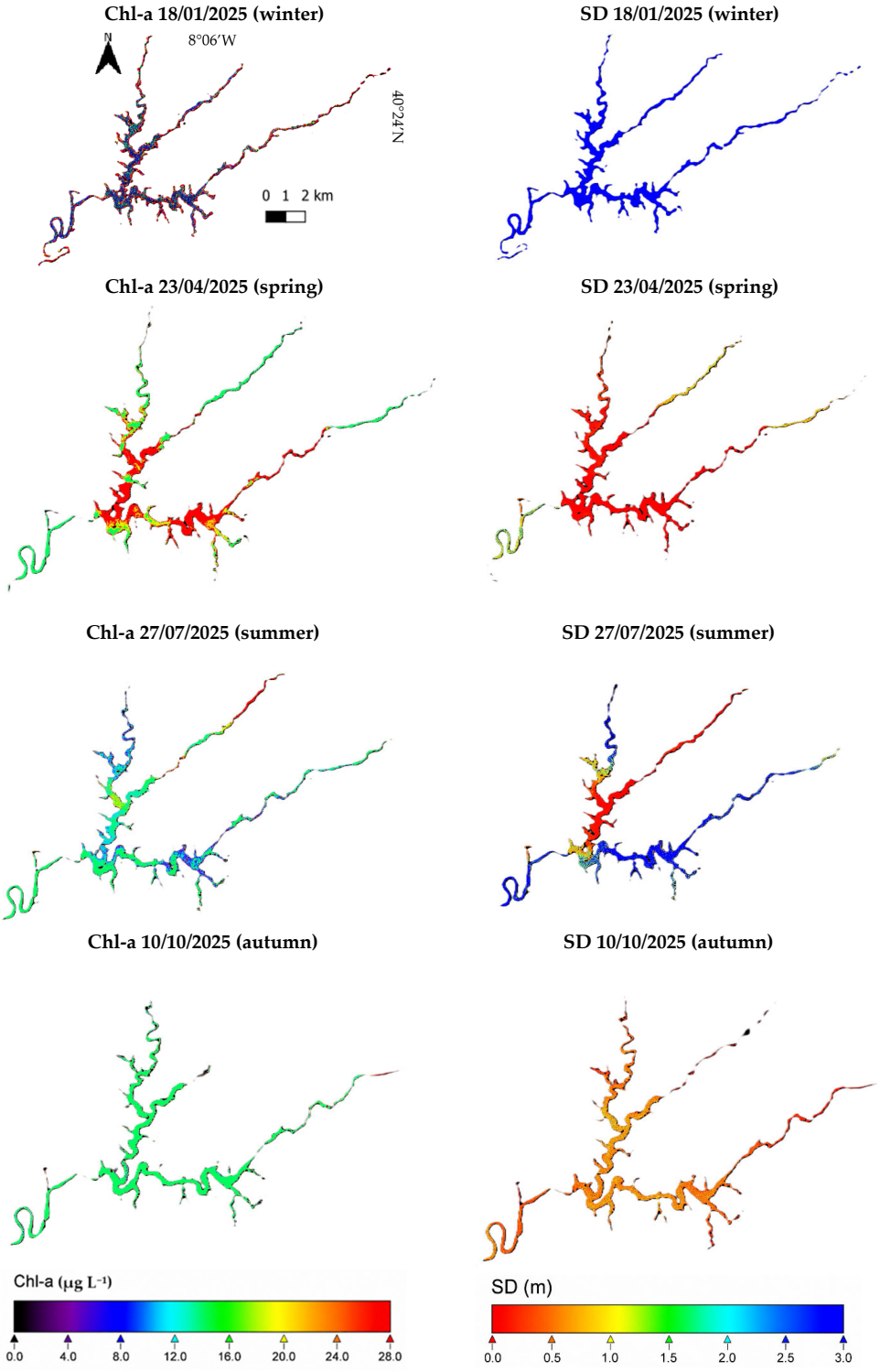


Figure 6. Spatial distribution maps of Chl-a and SD in the Ag Reservoir derived from Sentinel-2 L2A imagery, across different seasons in 2025.

4. Discussion

4.1. Integrated Dynamics of Water Quality

The results of this study highlight the complex and interconnected nature of water quality dynamics in inland reservoirs, reinforcing the need for integrated assessment approaches, as previously emphasized by Yang and Zhang et al. [2,31]. Clear differences emerged in the temporal behavior of key water quality parameters, indicating distinct ecological responses between reservoirs. The extreme environmental variability observed across the database, characterized by a coefficient of variation (CV) exceeding 99% for both Chl-a and SD, is highly representative of long-term monitoring in dynamic Mediterranean ecosystems. This exceptional statistical dispersion is primarily driven by the stark trophic contrast between the pristine, oligo-mesotrophic baseline of Rb and the anthropogenically pressured, eutrophic system of Ag. Furthermore, the extensive 10-year temporal frame (2014–2024) successfully captured severe hydroclimatic shifts in Portugal, ranging from intense winter runoff events that rapidly alter transparency to prolonged multi-year droughts that accelerate nutrient concentrations. When combined with episodic, high-magnitude summer phytoplankton blooms in the eutrophic system, these factors naturally generate a heavily right-skewed data distribution. This dynamic is mathematically supported by the high skewness (2.86) and kurtosis (12.6) values observed for Chl-a in Rb (Table 1), indicating a highly stable baseline that is occasionally punctuated by high-magnitude seasonal production events. Rather than indicating data instability, this wide operational spectrum provides a highly robust foundation for training and validating generally applicable remote sensing models.

In Rb, a significant increase in Chl-a concentrations was observed over the study period, accompanied by a significant decrease in water transparency. Together, these trends indicate a progressive shift toward more productive and turbid conditions, consistent with increasing phytoplankton biomass. This pattern suggests that internal biogeochemical processes and nutrient dynamics are driving changes in water quality over time, in line with the findings of Rodríguez-López et al. [7]. In contrast, although Ag exhibited consistently high Chl-a concentrations throughout the study period, no significant temporal trends were detected for either Chl-a or water transparency. These results indicate a stable condition over time, with persistently elevated productivity but without evidence of further increases or declines. The observed increase in Chl-a concentrations and the decline in SD in Rb indicate a gradual shift toward more productive and less transparent conditions over the study period. Although mean Chl-a concentrations remain within oligo- to mesotrophic ranges, the consistent upward trend (≈ 0.38 μg L^{-1} $year^{-1}$) suggests increasing phytoplankton biomass and enhanced nutrient availability. While direct chemical measurements of nutrient concentrations (such as total phosphorus or nitrogen) were not available for integration into this remote sensing framework, the coupled response of increasing Chl-a and declining SD serves as a robust, globally recognized optical proxy for gradual enrichment.

This pattern is consistent with classical limnological understanding, where increases in nutrient availability promote phytoplankton growth and reduce water clarity, as described in established frameworks such as those discussed by Sòria-Perpinyà et al. [23]. In Mediterranean systems like Rb, this progressive trajectory is typically associated with diffuse watershed pressures or internal loading from historical sediment stores during summer stratification [7]. The inverse relationship between Chl-a and SD observed in this study further supports this mechanism, indicating that phytoplankton dynamics are a major driver of light attenuation in the reservoir [4].

4.2. Performance and Limitations of Remote Sensing Models

The analysis of relationships between limnological variables demonstrated that Chl-a is the dominant driver of water transparency across the studied systems. The moderate and significant negative relationship between Chl-a and SD (R^2 = 0.31 for combined datasets) indicates that increases in phytoplankton biomass directly reduce light penetration. This relationship is consistent with optical classification frameworks, such as those reported by Spyrakos et al. [32], which distinguish inland waters based on their dominant optical constituents, including phytoplankton, suspended inorganic particles, and dissolved organic matter. These processes are also consistent with the findings of [13], who studied Albufera of València, a hypertrophic shallow lake, and demonstrated that Chl-a is a key determinant of water optical properties and SD variability. Their work showed that, under conditions of high nutrient inputs and strong phytoplankton development, temporal variations in Chl-a strongly control water clarity dynamics, a pattern directly comparable to those observed in the present study.

The spectral bands used in this study were selected based on known bio-optical properties of phytoplankton and inland waters [9,33]. The blue bands (443 nm and 490 nm, Sentinel-2 B1 and B2) are located in the Soret absorption maximum of Chl-a and are also sensitive to colored dissolved organic matter (CDOM), serving as a baseline for estimating phytoplankton absorption [22]. The green band (560 nm, B3) coincides with the maximum reflectance of water in the presence of phytoplankton and suspended particles, often used as a reference band in normalized indices [18]. The red band (665 nm, B4) corresponds to the maximum absorption peak of Chl-a in the red region, making it highly sensitive to variations in phytoplankton biomass [9]. The red-edge bands (705 nm and 740 nm, B5 and B6) capture the transition from strong chlorophyll absorption to high reflectance due to scattering by phytoplankton cells and fluorescence emission; these bands are particularly useful for higher chlorophyll concentrations [12,22].

The TBDO1 index ($R665 \times (1/R560 - 1/R443)$) exploits the strong absorption at 665 nm relative to the green reflectance peak (560 nm), while correcting for non-algal absorption using the blue band (443 nm) [23]. This configuration is well-suited for clear to moderately productive waters, such as the Rb reservoir. The TBDO index ($R740 \times (1/R665 - 1/R705)$) is specifically designed for more turbid, productive waters (e.g., the Ag reservoir), where the red-edge region provides improved sensitivity and minimizes interference from suspended inorganic particles [22,23]. The Maximum Chlorophyll Index (MCI) combines green, red, and blue bands to detect the reflectance peak associated with chlorophyll fluorescence, which is particularly evident in eutrophic systems [13,34]. The NDI (normalized difference index) between green and red bands captures the shift in water color from blue/green to green/yellow as phytoplankton biomass increases [24]. Thus, the spectral design of each index aligns with the optical characteristics of the two reservoirs, explaining the reservoir-specific performance observed in this study [9,12].

The empirical models developed using Sentinel-2 L2A reflectance data demonstrated moderate to high predictive performance, particularly for Chl-a concentration. The strongest predictive performance was observed for the reservoir-specific models, especially those developed for the Ag reservoir. The strong performance of the TBDO-based indices supports their suitability for estimating phytoplankton biomass in inland waters, consistent with previous findings by Sòria-Perpinyà et al. [23]. In their study, Chl-a was successfully retrieved from Sentinel-2 MSI imagery using atmospheric correction and field validation, with strong agreement between observed and estimated values ($R \approx 0.8$), confirming the robustness of satellite-based approaches for monitoring phytoplankton dynamics in optically complex inland waters.

Although the reservoir-specific models produced moderate mean absolute percentage errors (approximately 26–31%), this level of uncertainty aligns with results from other studies of optically complex inland waters, where multiple constituents influence the spectral signal [34]. The relatively high temporal variability of Chl-a, together with the influence of non-algal suspended particles (i.e., diverse seston), likely contributed to prediction errors, particularly at higher concentration ranges. Among the reservoir-specific models, predictive performance was consistently higher for the Ag reservoir than for the Rb reservoir. This difference can be explained by the contrasting optical regimes of the two systems. In Ag, higher Chl-a concentrations (mean = 11.2 μg L^{-1}) result in a reflectance spectrum that is strongly dominated by phytoplankton absorption and scattering, making the optical signal more predictable and closely coupled to Chl-a variations [9,23]. In contrast, Rb exhibits lower Chl-a concentrations (mean = 5.22 μg L^{-1}) and clearer waters, where the spectral signal is more influenced by other optically active constituents, such as non-algal particles, which introduce additional variability and reduce the relative contribution of phytoplankton to the water-leaving reflectance [8,32]. Consequently, lower phytoplankton dominance in Rb leads to a less predictable optical response and, therefore, lower model performance than in Ag.

This difference may be attributed to the higher Chl-a concentrations in Ag, which result in a reflectance spectrum dominated by phytoplankton absorption and scattering, strengthening the coupling between spectral indices and water transparency. In the clearer waters of Rb, the contribution of phytoplankton to the water-leaving reflectance is reduced, and other optically active constituents (e.g., non-algal particles) play a more significant role, increasing spectral variability and reducing the predictive performance of SD models [9,12,33,34]. Additionally, in very clear waters, SD may exceed the optical detection limit of Sentinel-2 (i.e., the signal may be dominated by bottom reflectance or water column attenuation becomes highly variable), further contributing to prediction uncertainties. In contrast, the more turbid conditions in Ag ensure that the water-leaving reflectance is primarily determined by within-water constituents, leading to more stable and predictable model performance for SD estimation.

A key finding of this study was the reduction in predictive performance observed when data from both reservoirs were combined into a single model. Compared with the reservoir-specific models, the combined-reservoir models exhibited lower predictive accuracy, indicating that the contrasting limnological and optical characteristics of the two systems limit model transferability. This result reinforces the importance of site-specific calibration when applying Sentinel-2-based empirical models across reservoirs with different trophic conditions [9].

The application of time-series cross-validation using a walk-forward approach demonstrated that the developed reservoir-specific and combined models exhibit good temporal stability and predictive robustness. The similarity between training and validation errors indicates minimal overfitting, supporting the models' reliability for future predictions. This validation strategy is particularly appropriate for environmental and remote sensing time series because it preserves the chronological order of observations, ensuring that models are trained exclusively on past data and evaluated on unseen future observations. Consequently, it avoids information leakage and provides a more realistic assessment of predictive performance under operational monitoring conditions. As highlighted by Vanhellemont and Tyler et al. [34,35], maintaining temporal consistency during model development and validation is essential for generating reliable long-term monitoring products and for assessing the temporal transferability of remote sensing models. Overall, the results confirm that, when properly calibrated and validated, remote sensing models can serve as effective tools for continuous water quality monitoring.

4.3. Integrated Spatiotemporal Assessment of Optical Water Quality Dynamics

Differences between the systems are also reflected in model performance. Higher predictive accuracy for Chl-a and SD in Ag suggests stronger consistency in the optical signal, particularly for indices such as TBDO and MCI. In contrast, the lower performance observed in Rb for SD may indicate more complex optical mixing conditions or reduced sensitivity of spectral indices under lower variability regimes. These findings are consistent with previous studies showing that model robustness in optically complex waters depends strongly on the relative dominance of phytoplankton versus non-algal particles [36,37].

The integrated analysis of spatial patterns, temporal trends, and inter-variable relationships provides a comprehensive view of the limnological dynamics of the studied reservoirs. Overall, the results reveal distinct ecosystem behaviors in Rb and Ag, reflecting differences in trophic condition and environmental variability. These findings are consistent with the ecological status assessments established under the Water Framework Directive (WFD), which classify Rb as Good and Ag as Moderate.

Spatially, both reservoirs exhibited an inverse relationship between Chl-a and SD, confirming the strong influence of phytoplankton biomass on water transparency. However, the spatial organization of this relationship is not static and varies according to seasonal hydrological conditions. During periods of heavy rainfall, runoff carries sediments and nutrients into the reservoirs, creating spatial gradients of turbidity and phytoplankton biomass. In these conditions, a longitudinal pattern often emerges, with higher Chl-a and lower SD near riverine inflow zones, followed by gradual water purification (i.e., sediment settling and nutrient uptake) along the reservoir toward the dam [9,23]. Conversely, during stable, rainless periods, reduced external inputs lead to more homogeneous spatial distributions of water quality parameters, as internal processes (e.g., phytoplankton growth, grazing, and vertical mixing) become dominant. Therefore, the apparent spatial heterogeneity or homogeneity observed in Figures 5 and 6 reflects the specific hydrological conditions preceding each image acquisition date, rather than fixed morphological characteristics of each reservoir. This dynamic behavior underscores the importance of accounting for seasonal and rainfall-driven variability when interpreting satellite-derived water-quality maps. Similar patterns have been reported in optically complex, more productive inland waters [9,12].

Temporal analyses further emphasized the contrasting dynamics of the two reservoirs. In Rb, increasing Chl-a and decreasing SD suggest a gradual decline in water transparency over time. Given the predominantly oligotrophic nature of this system, relatively small changes in phytoplankton biomass can be readily detected through optical indicators [9,38]. Conversely, the absence of significant trends in Ag does not necessarily indicate greater stability. Rather, the higher variability typically associated with eutrophic systems may obscure long-term directional changes, reducing their statistical detectability [39].

Taken together, the results suggest that Rb remains a relatively well-preserved system but may be experiencing subtle ecological changes that warrant continued monitoring. This is consistent with the characteristics of its watershed, which is smaller (5840 ha) and predominantly covered by undeveloped lands (47%) and traditional agricultural systems (26%), with low anthropogenic pressure (only one aquaculture facility) and proximity to the Peneda-Gerês National Park, a protected area [16]. These landscape features help buffer the reservoir against nutrient inputs and maintain good water quality.

Ag, in contrast, appears to operate under more productive, spatially heterogeneous conditions, consistent with its lower ecological classification (Moderate to Poor). Its watershed is approximately three times larger (19,123 ha) and is dominated by forest cover (75%), but largely composed of eucalyptus plantations for biomass production, which are associated with soil disturbance and nutrient runoff [16]. Moreover, the Ag watershed

experiences substantially higher anthropogenic pressure, including 27 urban wastewater treatment plants (WWTPs), 137 underground catchments (mostly for agriculture), and 89 surface water allocations for irrigation [16]. These contrasting watershed characteristics, smaller, protected, and less impacted in Rb versus larger, more intensively managed, and heavily pressured in Ag, explain the differences in water quality trends and remote sensing model performance observed between the two reservoirs.

The agreement between satellite-derived indicators and independent WFD assessments strengthens confidence in the observed patterns and highlights the potential of remote sensing as a complementary tool for long-term water quality monitoring and ecological status assessment. Furthermore, integrating remote sensing with watershed-scale landscape analysis, as demonstrated here, offers a more comprehensive framework for understanding the drivers of water quality degradation and supporting targeted management interventions.

4.4. Implications for Water Resource Management

The findings of this study have important implications for water resource management in the context of climate change and increasing anthropogenic pressure. The identification of early, subtle signs of eutrophication in the Rb reservoir underscores the need for preventive management strategies, particularly to control nutrient inputs.

The demonstrated ability of Sentinel-2 data to estimate key water-quality parameters provides a cost-effective, scalable complement to traditional monitoring programs. As emphasized by [8], remote sensing enables high-frequency, large-scale observations that are essential for detecting rapid changes and supporting decision making. Overall, integrating in situ measurements with satellite data is a powerful approach for adaptive, informed management of inland water systems, particularly in regions vulnerable to climate variability and water scarcity.

5. Conclusions

This study demonstrated that integrating in situ water-quality parameter data with Sentinel-2 L2A reflectance enables effective water-quality monitoring in Portuguese reservoirs and reveals contrasting ecological dynamics across systems. In the Rb reservoir, a significant increasing trend in Chl-a ($\approx$0.38 $\mu g\ L^{-1}\ year^{-1}$) coupled with decreasing water transparency provides strong evidence of progressive eutrophication, despite overall hydrological stability. In contrast, the Ag reservoir showed no significant long-term trends in Chl-a or SD, indicating a more stable optical regime.

Empirical models based on spectral indices (TBDO1, TBDO, MCI, NDWI) achieved moderate to high predictive performance, particularly for Chl-a (R^2 up to 0.75). Time-series cross-validation confirmed the robustness of these models ($R^2 \approx 0.67$–0.68), while the marked decline in performance when combining datasets ($R^2 \leq 0.45$) underscores the necessity of site-specific calibration. Paired statistical comparisons between modeled and observed values showed no significant differences ($p > 0.05$), supporting the overall reliability of the proposed approach for estimating Chl-a and SD depth in the studied reservoirs.

Overall, Sentinel-2 imagery is a cost-effective and scalable tool for supporting long-term water quality monitoring and management. The early detection of subtle eutrophication signals in Rb underscores the urgency of implementing preventive nutrient management strategies, particularly in reservoirs vulnerable to climate change and increasing anthropogenic pressures.

Author Contributions: Conceptualization, G.A.L. and S.C.A.; methodology, G.A.L.; software, G.A.L.; validation, G.A.L., S.C.A., C.G., G.P., G.R.C., X.S.-P., M.P. and J.D.; formal analysis, G.A.L.; investigation, G.A.L. and C.G.; resources, S.C.A.; data curation, G.A.L.; writing—original draft preparation,

G.A.L.; writing—review and editing, C.G., G.P., G.R.C., X.S.-P., M.P., J.D. and S.C.A.; visualization, G.A.L.; supervision, S.C.A., G.P., G.R.C., X.S.-P., M.P. and J.D.; project administration, S.C.A.; funding acquisition, S.C.A. All authors have read and agreed to the published version of the manuscript.

Funding: This research was funded by national funds through FCT—Fundação para a Ciência e a Tecnologia, I.P., and by the European Commission's Recovery and Resilience Facility, within the scope of UID/04423/2025 (https://doi.org/10.54499/UID/04423/2025), UID/PRR/04423/2025 (https://doi.org/10.54499/UID/PRR/04423/2025), and LA/P/0101/2020 (https://doi.org/10.54499/LA/P/0101/2020). This research was also funded by project "2Qua—Water Quality and Quantity, the challenge for the present and future" (ref. COMPETE2030-FEDER-0691700—https://doi.org/10.54499/2023.17517.ICDT) which is supported by European funds, through COMPETE2030, and by national funds, through the Foundation for Science and Technology (FCT, Portugal). This study also had the support of FCT through the project LA/P/0069/2020 granted to the Associate Laboratory ARNET (https://doi.org/10.54499/LA/P/0069/2020) by the "Contrato-Programa" UID/04050/2025 funded by FCT I.P. (https://doi.org/10.54499/UID/04050/2025). This study was financed in part by the Coordenação de Aperfeiçoamento de Pessoal de Nível Superior—Brasil (CAPES)—Finance Code 001.

Data Availability Statement: The original contributions presented in this paper are included in the article. Further inquiries can be directed to the corresponding author. The maps, scripts, and quantitative datasets supporting this study have been deposited in the DataRepositóriUM and are available at https://doi.org/10.34622/datarepositorium/TFICCJ.

Conflicts of Interest: The authors declare no conflicts of interest.

References

1. Sidibe, G.; Sumana, S.L.; Shuaibu, A.; Xu, L. Assessing synergistic impacts of climate change and anthropogenic stressors on freshwater ecosystems. *Biodivers. Conserv.* **2026**, *35*, 65. [CrossRef]
2. Yang, Y.; Wen, J.; Su, M.; Chen, Q. Integrating water quality and water quantity to diagnose the health of water metabolism systems in multi-core multi-level urban agglomerations. *Water Res.* **2025**, *282*, 123899. [CrossRef] [PubMed]
3. Kana, M.; Susan, M.A.; Madakka, M.; Jayaraju, N.; Pratyusha, C.V. Anthropogenic impact on biogeochemical cycles: Unraveling the human disruption: A preliminary review. In *Coastal Biogeochemistry and Ecosystem Shifts*; Ganugapenta, S., Badimela, U., Mejjad, N., Krishnan, K.A., Eds.; Springer: Cham, Switzerland, 2026; Volume 43, Chapter 1. [CrossRef]
4. Flörke, M.; Schneider, C.; McDonald, R.I. Water competition between cities and agriculture driven by climate change and urban growth. *Nat. Sustain.* **2018**, *1*, 51–58. [CrossRef]
5. Vörösmarty, C.J.; McIntyre, P.B.; Gessner, M.O.; Dudgeon, D.; Prusevich, A.; Green, P.; Glidden, S.; Bunn, S.E.; Sullivan, C.A.; Reidy Liermann, C.; et al. Global threats to human water security and river biodiversity. *Nature* **2010**, *467*, 555–561. [CrossRef] [PubMed]
6. Van Vliet, M.T.H.; Jones, E.R.; Flörke, M.; Franssen, W.H.; Hanasaki, N.; Wada, Y.; Yearsley, J.R. Global water scarcity including surface water quality and expansions of clean water technologies. *Environ. Res. Lett.* **2021**, *16*, 024020. [CrossRef]
7. Rodríguez-López, L.; Bravo Álvarez, L.; Aguilera-Fuentes, P.; Fagel, N.; Frappart, F.; Bourrel, L. Impacts of water quality and quantity in Lake Chapo in North Patagonia, Chile. *Eur. J. Remote Sens.* **2026**, *59*, 2616974. [CrossRef]
8. Chen, J.; Chen, S.; Fu, R.; Li, D.; Jiang, H.; Wang, C.; Peng, Y.; Jia, K.; Hicks, B.J. Remote sensing big data for water environment monitoring: Current status, challenges, and future prospects. *Earth's Future* **2022**, *10*, e2021EF002289. [CrossRef]
9. Matthews, M.W. A current review of empirical procedures of remote sensing in inland and near-coastal transitional waters. *Int. J. Remote Sens.* **2011**, *32*, 6855–6899. [CrossRef]
10. Mouw, C.B.; Greb, S.R.; Aurin, D.; DiGiacomo, P.M.; Gorman, M.; Lee, Z.; Twardowski, M. Aquatic color radiometry remote sensing of coastal and inland waters: Challenges and recommendations for development of future missions. *Remote Sens. Environ.* **2015**, *160*, 15–30. [CrossRef]
11. Warren, M.A.; Simis, S.G.; Martinez-Vicente, V.; Poser, K.; Bresciani, M.; Alikas, K.; Ansper, A. Assessment of atmospheric correction algorithms for the Sentinel-2A MultiSpectral Imager over coastal and inland waters. *Remote Sens. Environ.* **2019**, *225*, 267–289. [CrossRef]
12. Pahlevan, N.; Mangin, A.; Balasubramanian, S.V.; Smith, B.; Alikas, K.; Arai, K.; Barbosa, C.; Bélanger, S.; Binding, C.; Bresciani, M.; et al. ACIX-Aqua: A global assessment of atmospheric correction methods for Landsat-8 and Sentinel-2 over lakes, rivers, and coastal waters. *Remote Sens. Environ.* **2021**, *258*, 112366. [CrossRef]

13. Caballero, G.R.; Delegido, J.; Sòria-Perpinyà, X.; Sánchez-Pérez, L.; Ruiz-Verdú, A.; Alvado, B.; Durán, M.C.; Ortega, D.; Vicente-Pedrós, E.; Moreno, J. Water quality in clear water reservoirs of the Júcar basin with Sentinel-2 level L2A images. In Proceedings of the Fifth Conference on Geomatic Engineering, Valencia, Spain, 2–3 July 2025.
14. Mann, H.B. Nonparametric tests against trend. *Econometrica* **1945**, *13*, 245–259. [CrossRef]
15. Kendall, M.G. *Rank Correlation Methods*, 4th ed.; Griffin: London, UK, 1975.
16. Pinto, I.; Azevedo, L.; Antunes, S.C. Changes in regional practices and their effects on the water quality of Portuguese reservoirs. *Earth* **2025**, *6*, 29. [CrossRef]
17. Pinto, I.; Rodrigues, S.; Lage, O.M.; Antunes, S.C. Assessment of water quality in Aguieira reservoir: Ecotoxicological tools in addition to the Water Framework Directive. *Ecotoxicol. Environ. Saf.* **2021**, *208*, 111583. [CrossRef] [PubMed]
18. Lorenzen, C.J. Determination of chlorophyll and pheopigments: Spectrophotometric equations. *Limnol. Oceanogr.* **1967**, *12*, 343–346. [CrossRef]
19. Tukey, J.W. *Exploratory Data Analysis*; Addison-Wesley: Reading, MA, USA, 1977.
20. Draper, N.R.; Smith, H. *Applied Regression Analysis*, 3rd ed.; Wiley: New York, NY, USA, 1998. [CrossRef]
21. Durbin, J.; Watson, G.S. Testing for serial correlation in least squares regression: I. *Biometrika* **1950**, *37*, 409–428. [CrossRef] [PubMed]
22. Dall'Olmo, G.; Gitelson, A.A.; Rundquist, D.C. Towards a unified approach for remote estimation of chlorophyll-a in both terrestrial vegetation and turbid productive waters. *Geophys. Res. Lett.* **2003**, *30*, 1938. [CrossRef]
23. Sòria-Perpinyà, X.; Urrego, P.; Pereira-Sandoval, M.; Ruiz-Verdú, A.; Peña, R.; Soria, J.M. Monitoring the ecological state of a hypertrophic lake (Albufera of València, Spain) using multitemporal Sentinel-2 images. *Limnetica* **2019**, *38*, 457–469. [CrossRef]
24. Seber, G.A.F.; Wild, C.J. *Nonlinear Regression*; Wiley: Hoboken, NJ, USA, 2003.
25. Willmott, C.J.; Matsuura, K. Advantages of the mean absolute error (MAE) over the root mean square error (RMSE) in assessing average model performance. *Clim. Res.* **2005**, *30*, 79–82. [CrossRef]
26. Hyndman, R.J.; Athanasopoulos, G. *Forecasting: Principles and Practice*, 2nd ed.; OTexts: Melbourne, Australia, 2018. Available online: https://otexts.com/fpp2/ (accessed on 1 June 2026).
27. Ang, Y.; Shafri, H.Z.M.; Lee, Y.P.; Abidin, H.; Bakar, S.A.; Hashim, S.J.; Abdullah, R. A novel ensemble machine learning and time series approach for oil palm yield prediction using Landsat time series imagery based on NDVI. *Geocarto Int.* **2022**, *37*, 9865–9896. [CrossRef]
28. Shapiro, S.S.; Wilk, M.B. An analysis of variance test for normality (complete samples). *Biometrika* **1965**, *52*, 591–611. [CrossRef]
29. R Core Team. *R: A Language and Environment for Statistical Computing*; R Foundation for Statistical Computing: Vienna, Austria, 2023. Available online: https://www.r-project.org/ (accessed on 19 January 2026).
30. McFeeters, S.K. The use of the Normalized Difference Water Index (NDWI) in the delineation of open water features. *Int. J. Remote Sens.* **1996**, *17*, 1425–1432. [CrossRef]
31. Zhang, X.B.; Huang, S.; Hu, Y.P.; Li, G.; Li, W.J.; Yang, S.F. Integrative approaches to river ecosystem assessment and restoration: A review of methodologies and strategies for coherent implementation. *Environ. Monit. Assess.* **2026**, *198*, 139. [CrossRef] [PubMed]
32. Spyrakos, E.; O'Donnell, R.; Hunter, P.D.; Miller, C.; Scott, M.; Simis, S.G.H.; Neil, C.; Barbosa, C.C.F.; Binding, C.E.; Bradt, S.; et al. Optical types of inland and coastal waters. *Limnol. Oceanogr.* **2018**, *63*, 846–870. [CrossRef]
33. Neil, C.; Spyrakos, E.; Hunter, P.D.; Tyler, A.N. Corrigendum to "A global approach for chlorophyll-a retrieval across optically complex inland waters based on optical water types". *Remote Sens. Environ.* **2020**, *246*, 111837. [CrossRef]
34. Vanhellemont, Q. Adaptation of the dark spectrum fitting atmospheric correction for aquatic applications of the Landsat and Sentinel-2 archives. *Remote Sens. Environ.* **2020**, *239*, 111607. [CrossRef]
35. Tyler, A.N.; Hunter, P.D.; Spyrakos, E.; Groom, S.; Lucke, T.; Merchant, C.J. Developments in Earth observation for the assessment and monitoring of inland, transitional, coastal and shelf-sea waters. *Sci. Total Environ.* **2016**, *572*, 1307–1321. [CrossRef] [PubMed]
36. Odermatt, D.; Gitelson, A.; Brando, V.E. Review of constituent retrieval in optically deep and complex waters from satellite imagery. *Remote Sens. Environ.* **2012**, *118*, 116–126. [CrossRef]
37. Kutser, T.; Metsamaa, L.; Strömbeck, N.; Vahtmäe, E. Monitoring cyanobacterial blooms by satellite remote sensing. *Estuar. Coast. Shelf Sci.* **2006**, *67*, 303–312. [CrossRef]
38. Carlson, R.E. A trophic state index for lakes. *Limnol. Oceanogr.* **1977**, *22*, 361–369. [CrossRef]
39. Ansper, A.; Alikas, K. Retrieval of Chlorophyll *a* from Sentinel-2 MSI Data for the European Union Water Framework Directive Reporting Purposes. *Remote Sens.* **2019**, *11*, 64. [CrossRef]

Disclaimer/Publisher's Note: The statements, opinions and data contained in all publications are solely those of the individual author(s) and contributor(s) and not of MDPI and/or the editor(s). MDPI and/or the editor(s) disclaim responsibility for any injury to people or property resulting from any ideas, methods, instructions or products referred to in the content.